
Article:
Liu, D., Gu, D., Smyl, D. orcid.org/0000-0002-6730-5277 et al. (2 more authors) (2019) B-spline based sharp feature preserving shape reconstruction approach for electrical impedance tomography. IEEE Transactions on Medical Imaging, 38 (11). pp. 2533-2544. ISSN 0278-0062

https://doi.org/10.1109/tmi.2019.2905245

B-spline based sharp feature preserving shape reconstruction approach for electrical impedance tomography

Dong Liu, Danping Gu, Danny Smyl, Jiansong Deng and Jiangfeng Du

***Abstract*—This paper presents a B-spline based shape reconstruction approach for electrical impedance tomography (EIT). In the proposed approach, the conductivity distribution to be reconstructed is assumed to be piecewise constant. The geometry of the inclusions is parameterized using B-spline curves, and the EIT forward solver is modified as a set of control points representing the inclusions' boundary to the data on the domain boundary. The low order representation decreases the computational demand and reduces the ill-posedness of the EIT reconstruction problem. The performance of the proposed B-spline based approach is tested with simulations which demonstrate the most popular biomedical application of EIT: lung imaging. The approach is experimentally validated using water tank data. In addition, robustness studies of the proposed approach considering varying initial guesses, inaccurately known contact impedances, differing numbers of control points, and degree of B-spline are performed. The simulation and experimental results show that the B-spline based approach offers improvements in image quality in comparison to the traditional Fourier series based reconstruction approach, as measured by quantitative metrics such as relative size coverage ratio and relative contrast. Inasmuch, the proposed approach is demonstrated to offer clear improvement in the ability to preserve the sharp properties of the inclusions to be imaged.**

***Index Terms*—Electrical impedance tomography, shape reconstruction, sharp feature, B-spline curve, inverse problems.**

I. Introduction

ELECTRICAL impedance tomography (EIT) is a non-invasive and radiation-free medical imaging technique. Based on the application of alternate micro currents along a set of electrodes placed around the chest wall, EIT allows continuous tomographic imaging of the conductivity distributions inside the chest. EIT technology has been used in a wide spectrum in medicine ranging from breast imaging, gastric emptying and brain function to lung function. For a recent review of EIT technologies, see [1].

EIT reconstruction methods can be divided into statistical and deterministic methods. Within the statistical methods, a prior model for the target is written explicitly and the solution of the image reconstruction problem is sought via a posterior probability distribution [2], [3]. In deterministic methods, regularization techniques have usually been adopted in order to stabilize the inversion [4], [5] Most commonly, regularization methods impose (explicitly or implicitly) sophisticated prior knowledge by appropriately regularizing the unknown parameters utilizing some matrix norm. For example, quadratic regularization methods like the Tikhonov regularization applied in [6] are popular methods in EIT. Such methods confer stability to the reconstruction process, but limit the capability of describing sharp properties in the sought parameters. Another well-known class of regularization is total variation (TV) regularization, it specifically addresses the issue of stability without blurring the required sharp discontinuities [7], [8].

In many applications, such as medical imaging, it is known *a priori* that the target contains piecewise constant conductivity distribution and sharp features such as organ boundaries [9], [10], as well as approximate ranges for realistic conductivity values. The aforementioned prior knowledge can be formulated as a regularity constraint on the solution of EIT.

Methods applied to problems in this way are referred to as shape-based reconstruction methods. Such processes usually involve reformulating the problem of conductivity reconstruction as an inverse problem for a special geometrical representation of embedded objects. Among the approaches that have been applied are level sets [11]–[14], truncated Fourier series [15]–[18], shape perturbation method [19] and geometric constraint method [20], etc.

Bézier curve (which is a special case of a B-spline curve) based approaches have also been applied to estimate shape and phase boundary in EIT [21] and in electrical capacitance tomography (ECT) [22]. Due to the fact that the Bézier curve is a global presentation of the shape, it is sensitive to control point movement and cannot represent very complicated shapes. This means that changing the position of a single control point of the Bézier curve causes the entire curve to change. The Bézier representation has other main disadvantages. For

Manuscript received January 22, 2019; revised March 8, 2019; accepted March 12, 2019. This work was supported in part by the National Key R&D Program of China (Grant No. 2018YFA0306600), in part by the NNSFC (Grants No. 61871356, No. 81788101, No.11771420 and No. 11761131011), in part by the CAS (Grants No. GJJSTD20170001 and No. QYZDY-SSW-SLH004), and in part by the Anhui Initiative in Quantum Information Technologies (Grant No. AHY050000) and Anhui Provincial Natural Science foundation under Grant 1708085MA25. (Corresponding author: Dong Liu.)

D. Liu and J. Du are with Hefei National Laboratory for Physical Sciences at the Microscale and Department of Modern Physics, University of Science and Technology of China, Hefei 230026, China, Key Laboratory of Microscale Magnetic Resonance, University of Science and Technology of China, Hefei 230026, China, and also with Synergetic Innovation Center of Quantum Information and Quantum Physics, University of Science and Technology of China, Hefei 230026, China, e-mail: (dong.liu@outlook.com).

D. Gu and J. Deng are with School of Mathematical Sciences, University of Science and Technology of China, Hefei 230026, China.

D. Smyl is with Department Civil and Structural Engineering, University of Sheffield, Sheffield, UK.

D. Liu and D. Gu contributed equally to this work.

example, the number of control points is directly related to the degree of the Bézier curve. Therefore, to increase the complexity of the shape or surface of the curve by adding control points requires increasing the degree of the curve, which may result in oscillation and cause numerical instability. As the degree increases, the complexity and therefore the computational time increases. Meanwhile, due to the increased complexity, curves with high degree are more sensitive to roundoff errors. What's more, it is fairly difficult to squeeze a Bézier curve close to an edge with a sufficiently small radius of the control polygon, e.g., the boundary of the inclusions to be imaged in EIT. Therefore, their extension to complicated shapes is notoriously problematic.

Other spherical harmonics and modified B-spline based approaches are used to parameterize and reconstruct simple 3D inclusion surfaces in EIT [23] using the boundary element method (BEM), in which only a polar shaped object is considered, and the extension to non-polar shaped objects might be problematic. The main reason is that the spherical harmonics expansion cannot be used to model non-polar shapes, and if one uses modified B-splines for modeling non-polar shapes, one has to modify the process of modeling the surface. Despite this realization, B-splines have also proven robust in use cases such as the reconstruction of shape boundaries in ECT applications [24].

Our goal in this paper is to introduce and evaluate a cubic B-Spline based shape reconstruction approach for *absolute* EIT using the finite element method (FEM). The non-global behavior of B-spline curves provides local control of the curve shape and avoids changing the shape in a global way, and thus offers an improved ability to provide more control flexibility than Bézier curves. The reason for selecting cubic B-spline curves is that the cubic curve is most commonly used and it provides enough control for most geometric modeling applications without the drawbacks of higher-order curves. For example, a higher order curve is usually considered unnecessarily complex, making it easy to introduce undesired wiggles or lead to physical imperfections. On the other hand, very low-order curves (quadratic and linear) offer too little flexibility in controlling the curves. Whereas cubic curves offer an intermediate balance between overly geometrically-sophisticated and sensitive higher-order curves and low-order curve representations.

More precisely, in this paper, we use uniform cubic B-spline (UCBS) curves for representing inclusions' boundaries. In UCBS, once the control points are determined, the shape of the curve, i.e., the boundary shape of the inclusion, is determined. Meanwhile, the shape based reconstruction approach allows for incorporation of prior information on which the inclusion(s) are likely to be presented in the target, e.g., the lung position is roughly known in thorax monitoring, which may be utilized in selecting the initial locations of the control points. Therefore, UCBS would be a reasonable choice for shape boundary representation in EIT. In addition, UCBS has the propensity to produce cusps due to a local maximum of curvature produced away from the control points, which may offer opportunities to achieve sharp properties of the inclusions in EIT. For example, the sharp corner of a triangular-shaped object may be well tracked based on the ability of UCBS to produce cusps.

Following the common assumption in shape-based reconstruction methods, the conductivity distribution to be reconstructed is assumed to be piecewise constant meaning that the conductivity of each region is a constant value. We also assume the number of the inhomogeneities inside the volume are known *a priori* but their conductivity properties and their shape and location are not. The boundary of the object is parametrically represented by an UCBS curve with a small number of (unknown) control points, which are treated as variables. The EIT forward solver is then modified as a set of control points representing the anomaly boundary to the data on the domain boundary. The low order representation decreases the computational demand and reduces the ill-posedness of the EIT reconstruction problem.

To evaluate the accuracy of the B-spline based approach, we use numerical and experimental data to show the improvement of the B-spline based approach over the classical Fourier series based reconstruction. Simulation data is also used to show B-spline based reconstruction for EIT lung imaging. Since a variety of parameters determine the B-spline's appearance, the B-spline's complexity is mostly determined by the number of control points. Usually, this parameter is chosen by using intuitive trial-and-error-procedures, aiming to find a balance between simplicity of the curve and approximation quality. We have carried out sets of reconstructions to study the robustness of the proposed approach against different initial guesses, different number of control points and degree of B-spline. Moreover, the performance of the B-Spline based approach is studied with and without modeling error due to non-homogeneous background and inaccurately known contact impedances.

The rest of this paper is organized as follows. In Section II, we briefly review the EIT forward model. We discuss the shape representation using B-spline curve and Fourier series in Section III. The numerical simulations, experimental setup, the implementation details and robustness studies are detailed in Section IV. We present the results that show the improvement of the proposed approach over the traditional Fourier series based approach, and the discussions in Section V. Finally, the conclusions are drawn in Section VI.

II. Forward problem of EIT

Let Ω be an open bounded domain in $R^q(q = 2, 3)$ with a boundary $\partial\Omega$. We denote the set of electrodes by $\{e_\ell\}_{\ell=1}^{L}$, which are placed on the boundary $\partial\Omega$ and disjoint from each other. Electric currents I_ℓ are injected from L contact electrodes into the domain, inducing the electric potential $u(x)$ inside Ω. The forward problem can be modeled using the complete electrode model (CEM) [25], which consists of the Poisson equation

$$\nabla \cdot (\sigma(x)\nabla u(x)) = 0 \ , \ x \in \Omega, \tag{1}$$

This article has been accepted for publication in a future issue of this journal, but has not been fully edited. Content may change prior to final publication. Citation information: DOI 10.1109/TMI.2019.2905245, IEEE Transactions on Medical Imaging

and the boundary conditions

$$u(x) + z_\ell \sigma(x) \frac{\partial u(x)}{\partial \nu} = U_\ell, \ x \in e_\ell, \ \ell = 1, ..., L, \quad (2)$$

$$\int_{e_\ell} \sigma(x) \frac{\partial u(x)}{\partial \nu} \, \mathrm{d}S = I_\ell, \quad \ell = 1, ..., L, \quad (3)$$

$$\sigma(x) \frac{\partial u(x)}{\partial \nu} = 0, \quad x \in \partial\Omega \backslash \bigcup_{\ell=1}^{L} e_\ell, \quad (4)$$

where $\sigma(x)$ is the conductivity distribution, $x \in \Omega$ is the spatial coordinate, z_ℓ is the contact impedance; U_ℓ is the measured electrical potential at electrode e_ℓ; ν denotes an outward unit normal.

In addition, in order to ensure the existence and uniqueness of the solution, the current I_ℓ needs to meet the charge conservation condition

$$\sum_{l=1}^{L} I_\ell = 0, \quad (5)$$

and the potential ground level needs to be fixed, i.e

$$\sum_{l=1}^{L} U_\ell = 0. \quad (6)$$

The numerical solution of the forward model (1-6) is often based on FEM. Utilizing an additive Gaussian model for the measurement noise, the observation model becomes

$$V = U(\sigma) + \epsilon, \quad (7)$$

where vector V consists all the measured voltages, $U(\sigma)$ is the forward solution using FEM, and ϵ is additive Gaussian noise with mean ϵ^* and covariance Γ_ϵ. For details of FE approximation of CEM, see e.g., [26].

III. Boundary Expression using B-Spline Curves and Fourier Series

In this section, two different boundary expressions using B-spline curves and Fourier series are briefly introduced. As illustrated in Fig. 1, let us assume that the domain Ω is divided into disjoint and simply connected subregions A_j, i.e., $\Omega = \bigcup_{j=0}^{N_j} A_j$, where N_j is the number of subregions.

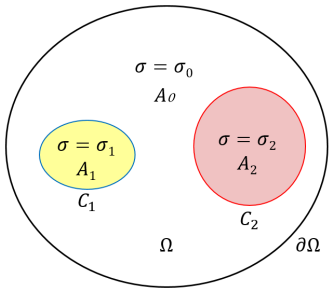

Fig. 1. Examples of subregion boundaries. C_1 and C_2 are used to denote the boundaries of the subregions A_1 and A_2, respectively. A_0 denotes the background region.

As we mentioned in Section I, the conductivity distribution in the domain was assumed to be piecewise constant, thus the conductivity distribution σ in the domain Ω can be written in the form

$$\sigma(x) = \sum_{j=0}^{N_j} \sigma_j \chi_j(x), \quad (8)$$

where $\chi_j(x)$ is a characteristic function of subregions A_j. For simplicity of presentation, we define a vector $\boldsymbol{\sigma}_{\text{pc}}$, including all the piecewise constant values in $\sigma(x)$, i.e.,

$$\boldsymbol{\sigma}_{\text{pc}} = [\sigma_0, \sigma_1, \cdots, \sigma_{N_j}]^T. \quad (9)$$

As a first step, FE mesh elements are classified into sets of elements inside the subregion A_j and those elements that intersect the region boundaries C_j, see Fig.2. For the elements that do not intersect the boundary are assigned their corresponding conductivity values σ_j, however, for the elements that lie on the boundary C_j, the area-weighted conductivity values, see details in [27], are assigned as

$$\sigma_{\text{ACD}} = \frac{\sigma_{\text{out}} S_{\text{out}} + \sigma_{\text{in}} S_{\text{in}}}{S_{\text{out}} + S_{\text{in}}}, \quad (10)$$

where footnotes marked as 'out' and 'in' denote outside and inside of the subregion A_j, respectively. S denotes the finite element area, and $S = S_{\text{out}} + S_{\text{in}}$, where $S_{\text{out}} = S_{\Delta\text{ABE}}$ and $S_{\text{in}} = S_{\text{BCDE}}$. We refer the readers to Fig. 2 for a schematic illustration of the above assignment of conductivity to curve crossing elements.

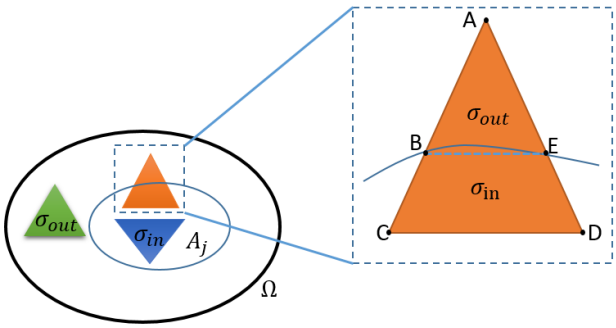

Fig. 2. Illustration of assignment of conductivity to curve crossing elements.

A. Uniform cubic B-spline based boundary representation

Given $n+1$ control points $p_0, p_1, \ldots, p_n$, the uniform cubic B-spline can be represented as a linear combination of basis functions, namely

$$C(t) = \sum_{i=0}^{n} p_i N_{i,k}(t), \quad (11)$$

where $N_{i,k}(t)$ is the i-th B-spline basis function of degree k (which is set as 3 in the paper), defined recursively as

$$N_{i,k}(t) = \frac{t - t_i}{t_{i+k} - t_i} N_{i,k-1}(t) + \frac{t_{i+k+1} - t}{t_{i+k+1} - t_{i+1}} N_{i+1,k-1}(t), \quad (12)$$

$$N_{i,0}(t) = \begin{cases} 1, & t_i \le t < t_i + 1, \\ 0, & otherwise. \end{cases} \quad (13)$$

where $i = 0, 1, \ldots, n$ and $\{t_i\}_{i=0}^{m}$ is a uniform knot vector with $m = n + k + 1$, defined as

$$t_i = \frac{i}{m}, \quad i = 0, 1, \ldots, m. \tag{14}$$

Equation (11) can be re-expressed in matrix form as

$$C = NP, \tag{15}$$

where N is a matrix composed of B-spline basis functions

$$N = \begin{pmatrix} N_{0,k}(q_0) & N_{1,k}(q_0) & \cdots & N_{n,k}(q_0) \\ N_{0,k}(q_1) & N_{1,k}(q_1) & \cdots & N_{n,k}(q_1) \\ \vdots & \vdots & \ddots & \vdots \\ N_{0,k}(q_M) & N_{1,k}(q_M) & \cdots & N_{n,k}(q_M) \end{pmatrix}, \tag{16}$$

where $\{q_i\}_{i=0}^{M}$ is a set of parameter values with $0 \leq q_0 < q_1 < \cdots < q_M \leq 1$ and M is a positive integer. Matrix P contains the (unknown) coordinates of control points, i.e.

$$P = \begin{pmatrix} p_{0,x} & p_{0,y} \\ p_{1,x} & p_{1,y} \\ \vdots & \vdots \\ p_{n,x} & p_{n,y} \end{pmatrix}. \tag{17}$$

To construct a closed B-Spline curve, we need to wrap the first k and last k control points. More precisely, let $P_0 = P_{n-k+1}$, $P_1 = P_{n-k+2}, \cdots, P_{k-2} = P_{n-1}$ and $P_{k-1} = P_n$.

Now, perturbing the control points will result in a change of conductivity distribution, so the space of unknown regions C_j is mapped into the space of unknown control points' coordinates P. Then, the observation model in (7) can be expressed as

$$V = U(\sigma(x, P)) + \epsilon. \tag{18}$$

Now, the problem of reconstructing the region boundary and estimating the piecewise constant conductivity vector $\boldsymbol{\sigma}_{\text{pc}}$ is equivalent to solving the following least square based minimization problem

$$[\hat{P}, \widehat{\boldsymbol{\sigma}_{\text{pc}}}] = \arg\min\{\|L_\epsilon(V - U(\sigma))\|^2 + \|L_p(P - P^*)\|^2 + \|\boldsymbol{\sigma}_{\text{pc}} - \boldsymbol{\sigma}_{\text{pc}}{}^*\|^2\}. \tag{19}$$

Here, L_ϵ is the Cholesky factor of the inverted noise covariance matrix Γ_ϵ^{-1} (i.e., $L_\epsilon^T L_\epsilon = \Gamma_\epsilon^{-1}$), the regularization matrix L_p is the Cholesky factorization of the matrix Γ_p^{-1} (i.e., $L_p^T L_p = \Gamma_p^{-1}$). P^* is a vector of *a priori* value of P and $\boldsymbol{\sigma}_{\text{pc}}{}^*$ are predetermined constant values, see details in Section IV-C.

B. Fourier representation

An alternative representation of a sufficiently smooth and closed boundary is to use the Fourier series [27], in which the boundary can be approximated in the form

$$C_j(s) = \begin{pmatrix} x_j(s) \\ y_j(s) \end{pmatrix} = \sum_{\omega=1}^{N_\theta} \begin{pmatrix} \gamma_\omega^{x_j} \theta_\omega^x(s) \\ \gamma_\omega^{y_j} \theta_\omega^y(s) \end{pmatrix} \quad j = 1, \cdots, N_j, \tag{20}$$

where $C_j(s)$ is the boundary of the j^{th} object (see Fig. 1). $\theta_\omega(s)$ are periodic differential basis functions and N_θ is the number of basis functions.

$$\theta_\omega^\alpha = 1, \quad \omega = 1, \tag{21}$$

$$\theta_\omega^\alpha = \sin\big(2\pi \frac{\omega}{2} s\big), \quad \omega = 2, 4, 6, \ldots, N_\theta - 1, \tag{22}$$

$$\theta_\omega^\alpha = \cos\Big(2\pi \big(\frac{\omega - 1}{2}\big) s\Big), \quad \omega = 3, 5, 7, \cdots, N_\theta. \tag{23}$$

Here $s \in [0, 1]$ and α refers to x or y. It follows from (20) to (23) that the boundaries C_j is identified with the vector γ of the shape coefficient, that is

$$\gamma = \begin{bmatrix} \gamma_1^{x_1}, \cdots, \gamma_{N_\theta}^{x_1} \\ \gamma_1^{y_1}, \cdots, \gamma_{N_\theta}^{y_1} \\ \cdots \\ \gamma_1^{x_{N_j}}, \cdots, \gamma_{N_\theta}^{x_{N_j}} \\ \gamma_1^{y_{N_j}}, \cdots, \gamma_{N_\theta}^{y_{N_j}} \end{bmatrix}, \tag{24}$$

where $\gamma \in \mathrm{R}^{2N_j N_\theta}$.

The inverse problem, therefore, becomes the estimation of $2N_j N_\theta$ Fourier coefficients γ together with the piecewise constant conductivity estimation

$$[\hat{\gamma}, \widehat{\boldsymbol{\sigma}_{\text{pc}}}] = \arg\min\{\|L_\epsilon(V - U(\sigma))\|^2 + \|L_\gamma(\gamma - \gamma^*)\|^2 + \|\boldsymbol{\sigma}_{\text{pc}} - \boldsymbol{\sigma}_{\text{pc}}{}^*\|^2\}. \tag{25}$$

Here, the regularization matrix L_γ is the Cholesky factorization of the matrix Γ_γ^{-1} (i.e., $L_\gamma^T L_\gamma = \Gamma_\gamma^{-1}$) and γ^* is a vector of *a priori* value of γ, see details in Section IV-C.

IV. Methods

In this section, the performance of the B-spine based approach is tested with numerical simulations and experimental data. The test cases, estimates, implementation details, parameter selection used in the computational methods and the experimental setup are explained. For the results and discussion, see Section V.

A. Simulation of EIT Measurements

To study the performance of the B-spline based approach, a circular domain with a radius of 14 cm and a chest-like domain were used for numerical studies. Sixteen electrodes were placed equidistantly on the boundary of the target domain. Currents were injected between electrodes i and j, $i = 1, 5, 9, 13, j = 1, \ldots, 16 \backslash i$, thereby generating a total of 54 pairwise current injections. The amplitude of the current was 1 mA, and the contact impedances z_ℓ were set to 5 Ω·cm for all the electrodes. The simulated conductivities of the tissues were set as 0.5 mS/cm for inflated lung, 1 mS/cm for deflated lung, 3 mS/cm for heart and 2 mS/cm for background. The discretization details of the measurement domain Ω in each of the test cases are given in Table I. In order to simulate real conditions, Gaussian noise with 0.1% standard deviation of the difference between the maximum and minimum value of the noiseless measurement data was added to the simulated data. The selected noise level corresponds to the signal to noise

TABLE I
DISCRETIZATION DETAILS OF THE MEASUREMENT AND RECONSTRUCTION DOMAINS IN THE TEST CASES. SECOND ORDER MESHES WERE USED FOR APPROXIMATING THE POTENTIAL $u(x)$, N_u AND N_e ARE THE NUMBER OF NODE POINTS AND ELEMENTS, RESPECTIVELY. N_e WAS ALSO USED FOR APPROXIMATION OF $\sigma(x)$.

	Simulated data		Reconstruction	
	N_u	N_e	N_u	N_e
Cases 1&2	9109	4466	6309	3082
Cases 3&4	7759	3764	7406	3587
	Experimental data		Reconstruction	
			N_u	N_e
Cases 5-7			6309	3082

ratio SNR $=$ 42dB, which represents well the noise level of modern EIT systems [28].

It is important to remark that, in the simulations, we did not use B-spline or Fourier series to represent the boundary of regions for assigning conductivity distributions. Rather, the regions of objects were manually located with a `MATLAB` script.

B. Experimental setup

In the experiments, a cylindrical tank with a diameter of 28 cm was filled with a saline solution having a conductivity of 0.543 mS/cm. Four different target conductivities were conducted by inserting non-conductive (plastic objects in Cases 4-6) and conductive inclusions (pumpkin and rutabaga in Case 7) with different shapes into the tank. All objects were translationally invariant in the vertical direction. Photos of all four targets are shown in Figs. 5&6(left column). The experiments were carried out using KIT4 measurement system [29]. The current patterns described in Section IV-A and adjacent measurement patterns were used in the measurements.

C. Implementation details

In the reconstructions, the initial guess of the region boundaries was manually set as circle or ellipse. More specifically, in the Fourier based reconstruction, we set the number of basis functions N_θ as 5, leading to a total of 10 Fourier coefficients, i.e., $\gamma \in \mathrm{R}^{10}$, for describing the initial curve $C_j(s)$ for each subregion A_j. In the B-spline based method, the number of control points $\mathrm{N_p}$ of each initial curve was set to $\mathrm{N_p} = n + 1 = 15$ for each inclusion, except in the robustness study of the proposed approach with respect to different number of control points in Section IV-D. That is, the dimension of unknown parameter $P \in \mathrm{R}^{2*N_p*N_j}$, i.e., $P \in \mathrm{R}^{30}$ for a single subregion. Note that, here, the number of control points does not include the number of duplicate points, as mentioned in Section III-A. Then, we choose 15 equal angular spacing points along the curve $C_j(s)$ as the control points to determine the B-spline curve. Within this strategy, the B-spline curve and the Fourier curve are almost identical. For this reason, we only show the initial B-spline curve in the reconstructed images.

The minimization problems in (19) and (25) were solved with an iterative Gauss-Newton optimization regime, which is equipped with a line-search algorithm to determine the step size λ_k in the solution $\hat{\theta}_k = \hat{\theta}_{k-1} + \lambda_k \bar{\theta}$. Here, $\hat{\theta}_k$ is the current estimate and $\bar{\theta}$ is the least square update. Such an approach requires the Jacobian $J_U(P, \boldsymbol{\sigma}_{\mathrm{pc}}) = \frac{\partial U}{\partial (P, \boldsymbol{\sigma}_{\mathrm{pc}})}$ for solving (19) and Jacobian $J_U(\gamma, \boldsymbol{\sigma}_{\mathrm{pc}}) = \frac{\partial U}{\partial (\gamma, \boldsymbol{\sigma}_{\mathrm{pc}})}$ for solving (25). According to the chain rule,

$$J_U(P) = \frac{\partial U}{\partial \sigma} \frac{\partial \sigma}{\partial P}, \tag{26}$$

and

$$J_U(\gamma) = \frac{\partial U}{\partial \sigma} \frac{\partial \sigma}{\partial \gamma}. \tag{27}$$

Here, the term $\frac{\partial U}{\partial \sigma}$ corresponds to the Jacobian computed using the standard method [6]. What needs to be determined is the second part $\frac{\partial \sigma}{\partial P}$ and $\frac{\partial \sigma}{\partial \gamma}$.

Since having a complex shape representation makes derivation of the Jacobian a tedious task, and for easy implementation purpose, the Jacobian matrix $\frac{\partial \sigma}{\partial P}$ in the B-spline based reconstruction is computed using perturbation method [30]. That is, each control point is perturbed in turn by a small value of epsilon and the corresponding change of voltage on each electrode is evaluated for approximation of Jacobian $\frac{\partial \sigma}{\partial P}$. The Jacobian matrix $\frac{\partial \sigma}{\partial \gamma}$ of the Fourier series based reconstruction was computed using a well-established method proposed in [27]. Finally, Jacobian matrix $J_U(\boldsymbol{\sigma}_{\mathrm{pc}})$ for both approaches can be easily computed using the standard method [6].

To determine the value of $\boldsymbol{\sigma}_{\mathrm{pc}}{}^*$ in the penalty term, we firstly computed the best homogeneous estimation $\widehat{\sigma^*_{\mathrm{hom}}} \in \mathbb{R}$ by solving

$$[\widehat{\sigma^*_{\mathrm{hom}}}] = \arg\min\{\|L_\epsilon(V - U(\sigma^*_{\mathrm{hom}}))\|^2\}, \tag{28}$$

and then we set $\sigma^*_0 = \sigma^*_{\mathrm{hom}}$ for the background conductivity, object conductivity $\sigma^*_{\mathrm{obj}} = \sigma^*_{\mathrm{hom}}$ for simulated studies and low-contrast experimental study, except in the robustness study of the proposed approach with respect to different initial piecewise constant conductivity values in Section IV-D. It should be noted, the EIT measurements are not sensitive to conductivity contrast above some limit [31], meaning that in a background of 0.1 mS/cm we may unable to distinguish between 1 mS/cm and 10 mS/cm. However, we may able to detect a conductivity 10 mS/cm in a 1 mS/cm background. For this reason, in the high-contrast experimental studies, we set $\sigma^*_{\mathrm{obj}} = \frac{1}{10}\sigma^*_{\mathrm{hom}}$, given the fact that the plastic objects have almost zero conductivity.

To quantitatively access the recovery of the shape using both B-spline and Fourier based methods, we computed the relative size coverage ratio (RCR), shown in Tables II&III, for the inclusions in the reconstructed images:

$$\mathrm{RCR} = \frac{\mathrm{CR}}{\mathrm{CR}_{\mathrm{True}}}, \tag{29}$$

where CR denotes the coverage ratio defined as the ratio of the size of the recovered inclusions to the total size of the measurement target, i.e., the experimental tank. Correspondingly, $\mathrm{CR}_{\mathrm{True}}$ is the CR of the true object. Value one would indicate exact match of size of the recovered and true inclusions, while a value less or greater than one would indicate underestimation or overestimation, respectively.

For quantitating the estimates of the binary conductivity values of both B-spline and Fourier based methods, a relative contrast (RCo) was calculated, shown in Tables II&III.

$$\mathrm{RCo}\sigma_j = \frac{\widehat{\sigma_j}}{\sigma_j^{\mathrm{True}}}. \tag{30}$$

For RCo, similarly to RCR, value one would indicate exact match of the true and estimated constant conductivity values, while a value greater or less than one would indicate overestimation or underestimation, respectively.

Note that in the experimental studies, we only computed the RCo for the background, i.e., saline, since the exact conductivity values of the inclusions are not known accurately.

D. Robustness studies of B-spline based approach in the presence of non-homogeneous background, different initial guesses, inaccurately known contact impedances, varying number of control points and degree

1) Non-homogeneous background: In practical applications, it is unrealistic to assume that the considered background are truly homogeneous. Instead of being constant, for example, the conductivity of heart is completely different to the background. For this reason, a more realistic value for the heart is assigned in Case 8, leading to a non-homogeneous background. As a result, Cases 3&8 offer a nice chance to study the performance of proposed approach with and without modeling errors due to the non-homogeneous background. It is important to remark that it is possible to apply one more B-spline curve or one more set of Fourier series for representing the region of heart. However, as our primary interest in this study is to investigate the performance of the proposed approach for persevering the sharp features in the potential EIT application– lung imaging, we defer this work to the future.

2) Differing locations of the initial curve: In solving nonlinear inverse problems, selection of proper initial guess for the curve's location and initial piecewise constant conductivity values are essential in achieving a stable and acceptable solution. To assess the robustness of the B-spline based approach to differing initial curve locations, we considered a set of reconstructions using the same data of Case 1, as shown in Fig. 8. In this test, the initial curve progressively moved towards the object in the target. To quantitatively describe the position of initial curve, we define a distance parameter dcc between the centers of the initial curve and the rectangle, i.e., large dcc means the initial curve far from the object, and vice versa. We refer the readers to Fig. 8 for a schematic illustration of the change of initial curve's location.

3) Different initial piecewise constant conductivity values: To explore the effect of initial piecewise constant conductivity values for the proposed approach, we performed a set of reconstructions of Case 3 (as shown in Fig. 10) by assigning different values to σ_1^*. For this purpose, we define

$$\sigma_1^* = \eta\sigma_{\mathrm{hom}}^*, \tag{31}$$

where η is the initial conductivity coefficient. With $\eta = [0.1, \cdots, 1]$, a total of 10 images were obtained. The evaluation parameters versus η were computed for all the images and are shown in Fig.9(middle).

4) Inaccurately known contact impedances: To study the effect of the B-spline based approach with respect to modeling errors caused by inaccurately known contact impedances, we considered a set of simulations by varying the contact impedances. To this end, the true contact impedances $\{z_\ell\}$ were generated by adding random Gaussian perturbations

$$z_\ell = |z_0 + \varepsilon_\ell|, \quad \varepsilon_\ell \sim \mathcal{N}(0, (\kappa z_0)^2) \tag{32}$$

to the nominal value $z_0 = 5\,\Omega$·cm. The contact impedances were simulated for 11 values of κ, $\kappa = 0, 0.1, 0.2, \ldots, 1$ and then these contact impedances were used to simulate EIT data from the target conductivity shown in top left of Fig. 11. An absolute value function was used to guarantee positivity of the contact impedances. The realization of z_ℓ in the case $\kappa = 0.4$ is shown in the bottom left of Fig.11. In the reconstruction, the contact impedances at all electrodes were assumed to be constant, i.e., $z_\ell \equiv z_0 = 5\,\Omega$·cm. The estimates for the case $\kappa = 0.4$ and the corresponding evaluation parameters RCRs and RCos for all the tests with $\kappa = 0, 0.1, 0.2, \ldots, 1$ are shown in the top right and bottom right of Fig.11, respectively.

5) Number of control points: The B-spline's appearance is largely determined by the control points, and consequently its complexity is determined by the number of control points, which is usually chosen quite arbitrarily by intuitive trial-and-error-procedures. To investigate the robustness of the proposed approach considering variability of the number of control points ($\mathrm{N_p}$), we computed a set of reconstructions for Case 5 with $\mathrm{N_p} = 4, \cdots, 27$ (as shown in Fig. 12). Note that for cubic curve, at least four control points are required to define a cubic curve. It is worth remarking that there are some other alternative ways for choosing the optimal number of control points, e.g., in [32], the task of choosing the optimal number was interpreted as a model selection problem based on the Bayesian information criterion. However, choosing the optimal number of control point in B-spline is out of the scope of this paper, hence it was left as a future research topic.

6) Degree: In this work, uniform cubic B-spline was used for representing object's boundary. An interesting question arises here: what is the performance of B-spline based reconstitution when the degree k of B-spline increases? For example, in some cases one might also be interested to check the performance with B-spline of degree higher than three. To get insight to this question, we carried out a set of reconstructions of Case 6 using odd-degree $k = 3, \cdots, 13$, shown in Fig.13. Note that, traditionally, odd-degree B-spline is more appropriate for interpolation problems, while even-degree B-spline is less suitable for it. Indeed, B-spline with even-degree leads to low quality interpolation and extreme sensitivity to data noise [33].

V. Results & discussion

In this section, we first show the comparison results for estimates based on B-spline and Fourier series, using numerical and experimental data. Then, we show the robustness studies of the B-spline based approach in the presence of

non-homogeneous background, different initial guesses, inaccurately known contact impedances, varying number of control points and degree.

A. Reconstructions from simulated data

Fig. 3 shows the results of Cases 1-3, where simulated data was studied, demonstrate that both B-spline and Fourier series based approaches successfully detect the locations of the inclusions. However, the quality of the estimates obtained with the proposed B-spline based approach is superior to the quality of Fourier series based estimate, especially for tracking the inclusions' shape. Further, the B-spline based approach is able to track the sharp corners of the inclusions, resulting the coverage ratios and relative contrasts closest to the true value for most of the test cases, see details in Table II. The Fourier series based estimate cannot recover the sharp corners, which is an expected result. The main reason is that the basis set of Fourier series is the smooth sinusoidal functions, which is optimized for expressing smooth rounded shapes. In other words, the use of (low order) Fourier series is not feasible in expressing the boundary with sharp corners.

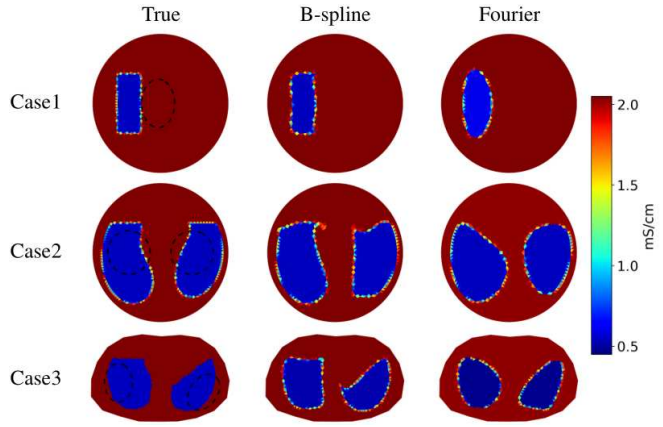

Fig. 3. Reconstructions with both B-spline based approach and Fourier series based approach from simulated data. The initial curves for each case are plotted as dashed line in the first column.

To explore the sensitivity to initial guesses of both approaches, we computed another set of reconstructions for Case 1 using different initial guess, as shown in Fig. 4. It can be seen that the Fourier series based reconstruction is highly sensitive to the initial guess, leading a poor reconstruction for the inclusion with a rectangle shape, see details in the first row of Fig. 4. On the other hand, the B-spline based reconstruction recovers the rectangle very well, and also appears to be relatively insensitive to the initial guess. Moreover, by visual inspection, the recovered value of the conductivity from the B-spline based approach is more accurate.

Note that for rectangular-shape estimation in Case 1, given a feasible selection of parameters in the anisotropic total variation regularization based reconstruction method, it is also possible to get reasonable reconstructions, see e.g., [8]. However, as pointed out in [8], the anisotropic TV regularization based approach strongly forces the inclusions' boundaries in the reconstructions to align along the coordinate axes, and thus, it may be a suitable choice in EIT only when the conductivity distribution is known a priori to feature such directional structures.

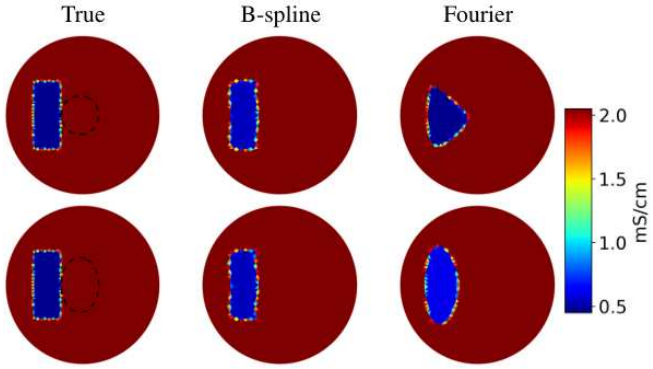

Fig. 4. Sensitivity study of the B-spline and Fourier series based approaches using different initial guesses. The initial guesses are plotted in the first column as dashed line. The same data set as Case 1 was used for the reconstruction and the second row is a repetition of the first row from Fig. 3.

B. Reconstructions from experimental data

Next, we proceed to reconstructions from water tank data. Fig. 5 depicts the results of both approaches on three high-contrast experimental test Cases 4-6. The resulting reconstruction images show better corner detection in the triangular and rectangular-shaped objects using the B-spline based approach. It can also be seen that the B-spline based approach produces a better reconstruction for a circular object in Case 5 than the Fourier series based approach, even though the uniform cubic B-spline is known to be unable to exactly represent a circle shape [34]. These findings are also supported by the evaluation parameters listed in Table III, the B-spline based approach leads most of those parameters closest to the true values. It is worth noting that reconstructing sharp angular boundaries of the triangular and rectangular-shaped objects is quite challenging in EIT, which has also been observed in [7], [12], [35]. Despite this reality, sharp angular boundaries can be more accurately detected by using the B-spline based approach, which encourages applying B-spline based shape reconstruction method to EIT reconstruction. For a comparison to isotropic and anisotropic TV regularization based reconstructions, performed on similar EIT data, we refer the readers to Fig. 8 in the recent work [8].

Fig. 6 shows the results of both approaches on one low-contrast experimental test Case 7. Again, both methods are able to detect the inclusions, although the contrast of the inclusions w.r.t the background is much smaller than Cases 4-6. Based on a visual assessment, B-spline based approach gives the better reconstruction, leading to a coverage ratio closer to the true value, RCR_U and RCR_D being 1.55 and 0.93, respectively.

C. Results of robustness studies

1) Effect of non-homogeneous background: Fig. 7 shows that the performance of both approaches in Case 8 compared to each other remains similar to the more ideal Case 3; the B-spline based approach gives again successful reconstructions

TABLE II
THE RCRS AND THE RELATIVE CONTRAST VALUE (RCO) OF THE RECONSTRUCTED σ_j IN THE SIMULATED STUDIES.

	Case 1			Case 2				Case 3				Case 8			
	RCR	RCoσ_0	RCoσ_1	RCR$_L$	RCR$_R$	RCoσ_0	RCoσ_1	RCR$_L$	RCR$_R$	RCoσ_0	RCoσ_1	RCR$_L$	RCR$_R$	RCoσ_0	RCoσ_1
True	1.00	1.00	1.00	1.00	1.00	1.00	1.00	1.00	1.00	1.00	1.00	1.00	1.00	1.00	1.00
Fourier	1.02	1.00	1.05	0.99	0.96	0.98	0.97	0.89	0.92	0.98	0.82	0.86	0.87	0.98	0.86
B-spline	0.97	0.99	0.99	0.98	0.99	0.99	1.00	0.96	0.99	1.00	0.95	0.88	0.91	1.00	0.88

* The subscript letters 'L' and 'R' under the parameter RCR denote the left and right side objects in the domain, respectively.

TABLE III
THE RCRS AND THE RELATIVE CONTRAST VALUE (RCO) OF THE RECONSTRUCTED σ_j IN THE EXPERIMENTAL STUDIES.

	Case 4		Case 5			Case 6			Case 7		
	RCR	RCoσ_0	RCR$_L$	RCR$_R$	RCoσ_0	RCR$_L$	RCR$_R$	RCoσ_0	RCR$_U$	RCR$_D$	RCoσ_0
True	1.00	1.00	1.00	1.00	1.00	1.00	1.00	1.00	1.00	1.00	1.00
Fourier	1.12	0.99	1.14	1.91	1.00	1.10	1.67	1.00	2.04	2.64	0.99
B-spline	1.07	0.99	1.05	0.99	1.01	1.14	0.92	1.01	1.55	0.93	0.99

* The subscript letters 'U' and 'D' under the parameter RCR denote the upside and downside objects in the low-contrast case, respectively.

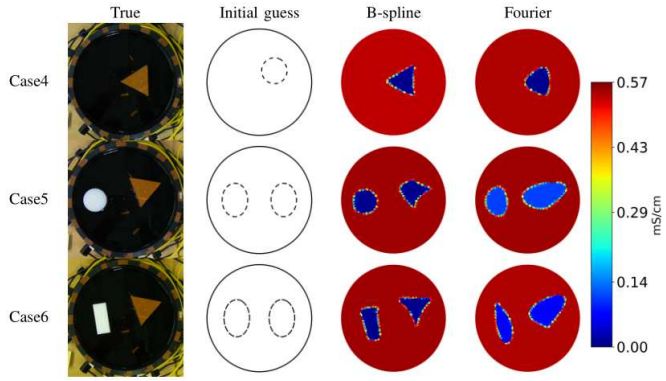

Fig. 5. Reconstructions with both B-spline based approach and Fourier series based approach from *high-contrast* experimental data. The initial curves for each case are plotted as dashed line in the second column.

of the shape of lungs and the sharp corners, leading to the RCR and RCo index closest to the true value, see Table. II. We note that the RCR of the proposed approach is slightly underestimated, which doesn't exceed our expectation, due to the modeling errors caused by the non-homogeneous background.

It should be noted that there is a cusp (which is not present in the true images) in the right lung of both Cases 3& 8. This stems from the fact that the propensity to produce cusps is due to a local maximum of curvature being produced away from the control points. One may consider incorporating curvature constraints, e.g., by setting the maximum curvature [36], along the B-spline curve to avoid it, and/or to apply angle-constrained manipulation for the B-spline curve.

2) Effect of initial curve's location: Two representative results of $dcc = 7$ and 9.5 cm are shown in Fig. 8, and all

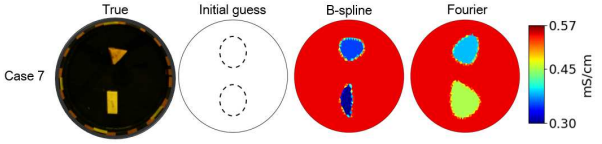

Fig. 6. Reconstructions with both B-spline based approach and Fourier series based approach in *low-contrast* experiments with rutabaga and pumpkin. The initial curves are plotted as dashed line in the second column.

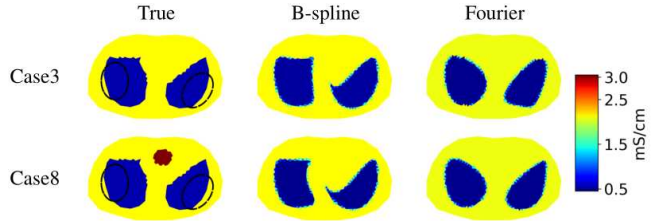

Fig. 7. Reconstructions with both B-spline based approach and Fourier series based approach for simulated Lung imaging with and without non-homogeneous background. The first row is a repetition of the 3rd row from Fig. 3.

the evaluation parameters RCR and RCos versus the distance parameter dcc are plotted in Fig. 9 (left column). Based on these results, we can conclude that the proposed approach is quite robust to the varying location of initial curve, resulting very good reconstructions of the rectangular-shape and detection of the sharp corner.

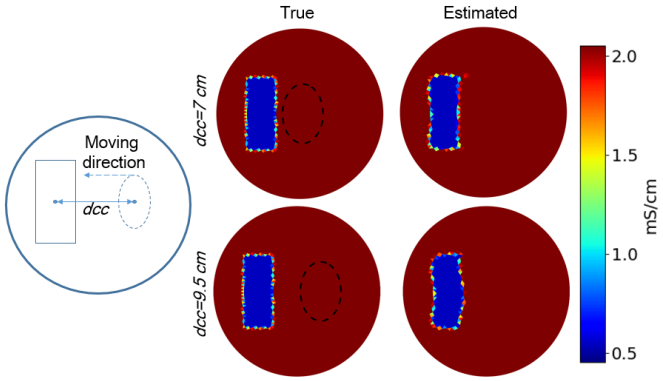

Fig. 8. Robustness study of the B-spline based approach w.r.t different initial curve's location. The same data set as Case 1 was used for the reconstruction.

3) Effect of initial piecewise constant conductivity values: Two representatives from 10 images are shown in Fig.10, it can be seen that the lung shapes are well tracked. Further, the sizes are feasible and the final piecewise conductivity values are accurately estimated, which is supported by the evaluation parameters RCR and Rco plotted in Fig.9(middle).

4) Effect of inaccurately known contact impedances: The results show that, in the presence of a contact impedance bias, image reconstruction is still feasible with a fixed constant contact impedance. This is a nice feature from a practical point of view, since medical EIT is always accompanied by modeling errors caused by inaccurately known contact impedance. As an example, during thorax monitoring with EIT, the contact impedance of electrodes may change significantly due to drying of the electrode gel and sweat on the skin.

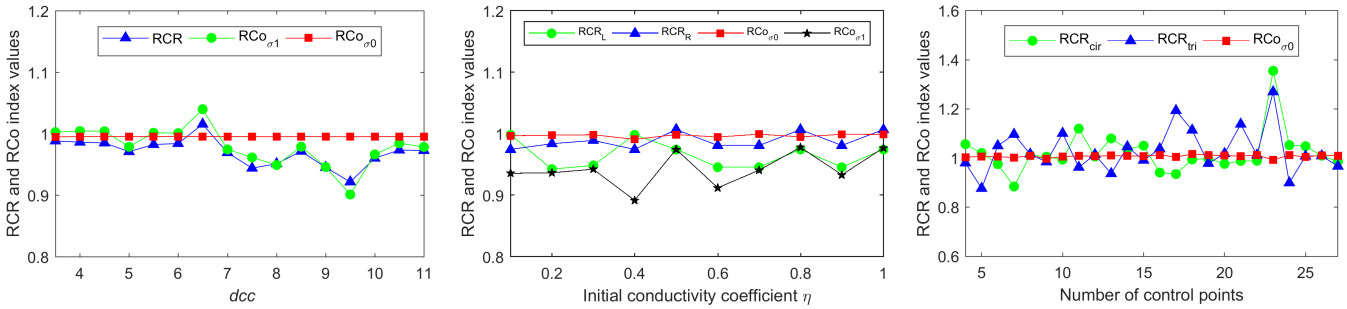

Fig. 9. Evaluation parameters of the robustness studies. Left: parameters versus the distance *dcc* between the centers of the initial curve and the inclusion studied Sec. V-C2; Middle: parameters versus the initial conductivity coefficient η of the cases studied in Sec. V-C3; Right: parameters versus the number of control points of the robustness studies in Sec. V-C5.

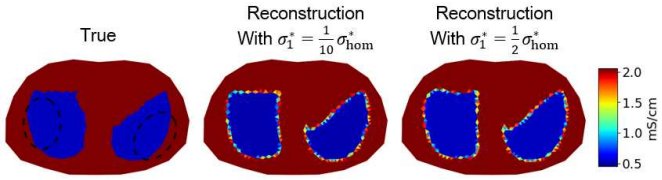

Fig. 10. Robustness study of the B-spline based approach w.r.t different initial piecewise conductivity value. The same data set as Case 3 was used for the reconstruction.

We note that there has been previous work addressing the problem of unknown/uncertain contact impedances: In [37], the contact impedances were simultaneously estimated with the conductivity distribution; in [38], the uncertainties of the contact impedances were modeled statistically and then compensated by employing the so-called approximation error method (AEM) [3]. For an extensive study of the effect of time-varying contact impedance in EIT, we refer to the recent publication in [39].

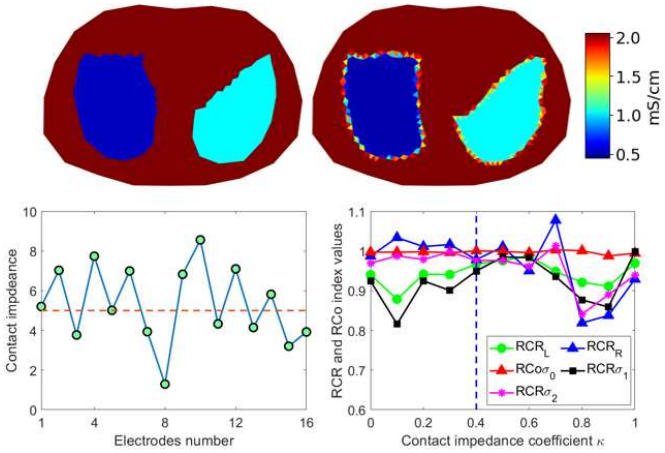

Fig. 11. Robustness study of the proposed approach *w.r.t* contact impedance z_ℓ. Top left: True conductivity. Top right: B-spline based reconstruction. Bottom left: simulated contact impedances z_ℓ in the case of $\kappa = 0.4$, the dashed horizontal line indicates the fixed $z_\ell \equiv z_0 = 5\,\Omega \cdot \text{cm}$ for the reconstruction shown in the top right. Bottom right: RCR and RCo index values versus contact impedance coefficient κ, the dashed vertical line denotes the case shown in the top row.

5) Effect of the number of control points: Fig. 12 shows the results of robustness of B-spline based reconstructions against different number of control points N_p. It is clear that the B-spline based approach is quite robust to the number of control points, where most cases were well reconstructed, especially for the triangular-shaped object with sharp corners. Note that distortions are introduced in few cases, e.g., $N_p = 19, 27$, which might be related to the ill-posedness of the EIT reconstruction problem. When N_p is selected as a small value, e.g., $N_p = 8$, the dimension of unknown parameter P is $\mathrm{R}^{2*N_p*N_j}$, i.e., $P \in \mathrm{R}^{32}$. When N_p turns to be a relatively large value, e.g., $N_p = 26$, the dimension of unknown parameter P increases to R^{104}. This implies that the reconstruction problem becomes increasingly *ill posed* as the unknowns increase, comparing to the less ill posed situation where relatively few control points are used. It is worth remarking that, in this paper, the selection of N_p was done by trial and error and is therefore not optimal. Better selection of this parameter may be conducted by taking into account the relative trade-offs with the data discrepancy norm, convergence rate of the minimization problem, etc. Further, by visual inspection, the reconstruction performance to the circular-shaped object is slightly biased. This may be explained by the fact that uniform cubic B-splines cannot be used to accurately express common conic shapes such as circles, ellipses, etc, in principle [34]. Nevertheless, within such a large range of the number of control points in this test case, the reconstruction performance is still acceptable, which is also evident from the evaluation parameters plotted in Fig. 9 (right column).

6) Effect of B-spline's degree: It can be seen that the cubic ($k = 3$) B-spline based reconstruction shows superior performance and tracks the shape of the inclusions reasonably well, as evidenced by the evaluation parameters shown in Fig. 14. On the other hand, wiggles are produced when degree k increases, causing shape distortions to the reconstructed images. In short, we found that the B-spline of degree $k = 3$ assure good compromise between the reconstructed image quality and the computational complexity, while higher degree splines cause shape distortions and also compromise the lower computational complexity. This is also consistent with the text mentioned in Section I.

Note that in Fig. 13, the inclusions are quite simple, but in real applications, organs are more complex. For this reason, we also tried one additional set of robustness studies of the B-spline degree k for the test case with more complicated inclusions shown in Fig. 11, we found that it was comparable to the experimental example shown in Fig. 13. Due to the

This article has been accepted for publication in a future issue of this journal, but has not been fully edited. Content may change prior to final publication. Citation information: DOI 10.1109/TMI.2019.2905245, IEEE Transactions on Medical Imaging

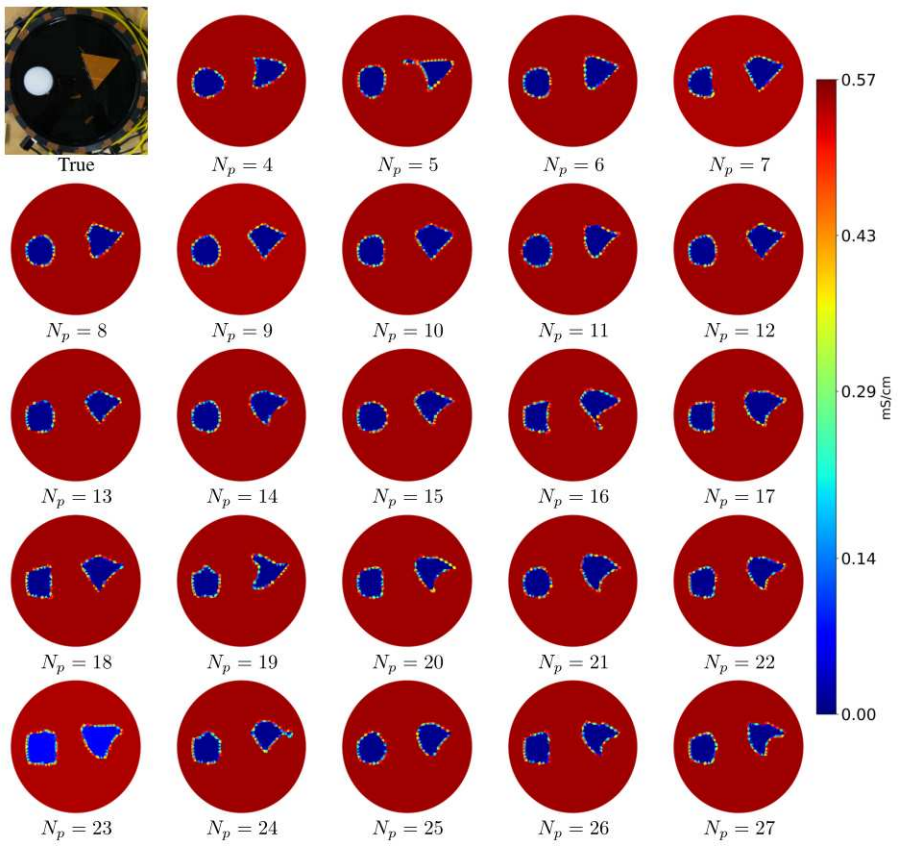

Fig. 12. Robustness study of the B-spline based estimate with respect to the number of control points. The same experimental data and initial guesses in Case 5 were used for the reconstruction.

space limitation, we didn't show the reconstructed images.

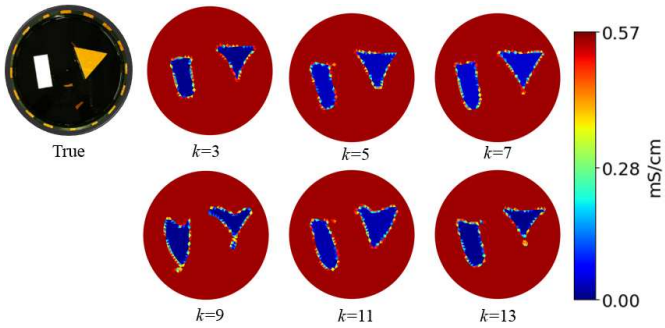

Fig. 13. Robustness study of the B-spline based estimate with respect to the B-spline degree k. The same experimental data and initial guesses in Case 6 were used for the reconstruction.

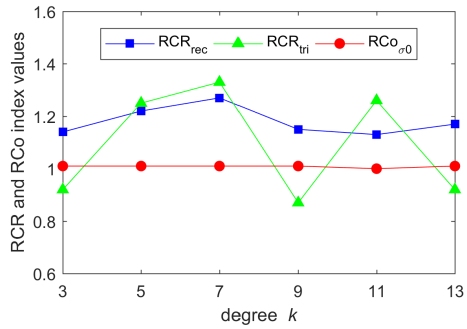

Fig. 14. Evaluation parameters of the robustness studies of the B-spline based estimate with respect to degree k.

D. Discussion on the results

As mentioned in Section IV-C, the Jacobian matrix $\frac{\partial \sigma}{\partial P}$ in (26) was computed using the perturbation method. It is well known that perturbation method can introduce inaccuracies in the Jacobian computation [40], which may significantly affect the nonlinear reconstruction problem. However, the results demonstrate that the B-spline based reconstruction tolerates such errors well, leading quite reasonable shape reconstructions and preserving the sharp features. Further, the B-spline based approach also has good robustness against the initial guesses and numbers of control points.

At last, it should be noted that for uniform cubic B-spline, the basis functions depend on a series of knots can just be set to equally spaced integers, and every control point is equally weighted. Very often in practical applications, one may have interest in extremely flexible geometric representations through estimating or setting the values of associated weights, adjusting the positions of the control points, choosing the knots adaptively and modifying the knot vector distribution. This brings forth the idea of applying non-uniform B-spline [41] and non-Uniform Rational B-Spline [42] to shape reconstruction in EIT, which will be investigated in future work.

E. Limitations and further developments

The present work is limited in that it is based in the context of *absolute imaging*. As such, there are several issues that need mentioning.

- First, the proposed approach is intrinsically sensitive to modeling errors arising from electrodes' displacement and inaccurate knowledge of the domain boundary shape. In other words, the reconstruction ability is highly dependent on the *a priori* information of the electrode positions and domain boundary shape. One potential solution is to apply AEM to compensate such modeling errors [43]. Framing the reconstruction approach in the context of *linear difference imaging* or *nonlinear difference imaging* would be another potential solution. This is because difference imaging tends to be quite robust to these sources of modeling errors, which are largely canceled out in the measurement subtraction and absorbed by the background estimation using the nonlinear approach [44], [45].
- Second, the cost in each iteration of the proposed approach, in terms of time, is slightly more than the Fourier series based approach. This is because the dimensionality of the unknowns in the proposed approach is larger than the Fourier series based approach. As an example, the estimate of Case 1 was obtained from a MATLAB implementation of the proposed approach on a desktop PC with an Intel Xeon E3-1231 processor and 16GB memory within 8 iterations at average speed of 43 seconds/iteration. As a comparison, implementation of Fourier series based approach carried out on the same PC within 6 iterations at average speed of 39 seconds/iteration. To compare the convergence behavior of both approaches, in Fig. 15 we show the root mean square error (RMSE) of the estimated conductivity distribution against the iteration steps for both methods in Case 1. Both reconstructions terminate when there is no further reduction on the cost functions. In short, time cost of the proposed approach is comparable to the Fourier series based approach. We remark that the computational time required for each test case would vary depending on a number of factors, including the number of control points, initial guess and stopping criteria, etc. Note that, as in traditional finite element based non-linear iterative methods, a line search is also performed on the estimation. This process demands repetitive calculation of the forward problem, and a key challenge in practical applications is to reduce the computing time without sacrificing the accuracy of the solution. One possible way is to apply AEM in the Bayesian framework for solving inverse problems, since AEM offers a good chance to attain a feasible resolution in a coarse discretization by treating the modeling error produced by discretization as an unknown that is estimated as part of the inverse problem [38].
- In addition, for all the test cases studied in this paper, we assumed that all the subregions presented in the background are simply disconnected. However, one may argue that this assumption is probably unjustified, e.g, in real applications, some cancers that may appear as a mass in the lungs include lymphomas and sarcomas, which should be treated as a nested case. In principle, given the assumption that mass is known to be nested in the lung, the proposed approach is able to handle the situation of detecting nested inclusions by modeling the mass using one B-spline curve and the lung shape using the other B-spline curve. However, in practice, the B-spline curve of a nested inclusion often moves outside of the surrounded inclusion, such that instability is likely to recur. From a practical point of view, to apply the proposed approach for reconstructing nested inclusions, we suggest the incorporation of more prior information to improve the stability of the iterative inversion. For example, if an inclusion is known to be nested inside another, this can be used *a priori* information for initially setting one B-spline curve inside another. One may also consider defining a region-of-interest using an *a priori* span, then B-splines can be sculpted to have desirable shapes and can be made to vanish outside the span. In other words, without such *a priori* information, the reconstruction problem is unstable due to mutual interactions between two B-spline curves. In addition, another potential solution for nested inclusion reconstruction is to apply multiple level set functions for modeling conductivity distribution with nested inclusions.

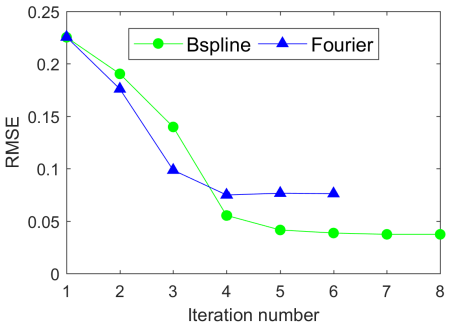

Fig. 15. Root mean square error reduction through the iterative process of Case 1 shown in Fig.3.

VI. Conclusion

In this paper, we proposed a B-spline based shape reconstruction approach for electrical impedance tomography. The proposed approach was evaluated using simulations and phantom studies. We found that the B-spline based approach provides more accurate reconstructions of the object's shape and better preserves sharp features than the conventional Fourier series based approach. It has been shown that the proposed approach tolerates modeling error caused by non-homogeneous backgrounds and inaccurately known contact impedances, and is relatively insensitive to initial guesses, number of control points and degree of B-spline. The findings demonstrate that, given the assumption that the properties of conductivity distribution are piecewise constant, the proposed approach is not only robust, but also has significant potential to be a generalized method for incorporating shape prior information in EIT image reconstruction.

References

[1] A. Adler and A. Boyle, "Electrical impedance tomography: Tissue properties to image measures," *IEEE Transactions on Biomedical Engineering*, vol. 64, no. 11, pp. 2494–2504, 2017.

[2] S. Liu, J. Jia, Y. D. Zhang, and Y. Yang, "Image reconstruction in electrical impedance tomography based on structure-aware sparse bayesian learning," *IEEE Transactions on Medical Imaging*, vol. 37, no. 9, pp. 2090–2102, 2018.

[3] J. Kaipio and E. Somersalo, *Statistical and computational inverse problems*. Springer Science & Business Media, 2006, vol. 160.

[4] X. Chen, *Computational Methods for Electromagnetic Inverse Scattering*. John Wiley & Sons, 2018.

[5] J. L. Mueller and S. Siltanen, *Linear and nonlinear inverse problems with practical applications*. Siam, 2012, vol. 10.

[6] M. Vauhkonen, D. Vadasz, P. A. Karjalainen, E. Somersalo, and J. P. Kaipio, "Tikhonov regularization and prior information in electrical impedance tomography," *IEEE transactions on medical imaging*, vol. 17, no. 2, pp. 285–293, 1998.

[7] G. González, J. Huttunen, V. Kolehmainen, A. Seppänen, and M. Vauhkonen, "Experimental evaluation of 3d electrical impedance tomography with total variation prior," *Inverse Problems in Science and Engineering*, vol. 24, no. 8, pp. 1411–1431, 2016.

[8] G. González, V. Kolehmainen, and A. Seppänen, "Isotropic and anisotropic total variation regularization in electrical impedance tomography," *Computers & Mathematics with Applications*, vol. 74, no. 3, pp. 564–576, 2017.

[9] S. J. Hamilton, J. L. Mueller, and M. Alsaker, "Incorporating a spatial prior into nonlinear d-bar eit imaging for complex admittivities," *IEEE Trans. Med. Imaging*, vol. 36, no. 2, pp. 457–466, 2017.

[10] M. Alsaker and J. L. Mueller, "Use of an optimized spatial prior in d-bar reconstructions of eit tank data," *Inverse Problems & Imaging*, vol. 12, no. 4, pp. 883–901, 2018.

[11] M. Soleimani, O. Dorn, and W. R. Lionheart, "A narrow-band level set method applied to eit in brain for cryosurgery monitoring," *IEEE transactions on biomedical engineering*, vol. 53, no. 11, pp. 2257–2264, 2006.

[12] D. Liu, A. K. Khambampati, and J. Du, "A parametric level set method for electrical impedance tomography," *IEEE Transactions on Medical Imaging*, vol. 37, no. 2, pp. 451–460, 2018.

[13] D. Liu, D. Smyl, and J. Du, "A parametric level set based approach to difference imaging in electrical impedance tomography," *IEEE transactions on medical imaging*, vol. 38, no. 1, pp. 145–155, 2019.

[14] D. Liu, Y. Zhao, A. K. Khambampati, A. Seppanen, and J. Du, "A parametric level set method for imaging multi-phase conductivity using electrical impedance tomography," *IEEE Transactions on Computational Imaging*, vol. 4, no. 4, pp. 552–561, 2018.

[15] V. Kolehmainen, A. Voutilainen, and J. P. Kaipio, "Estimation of non-stationary region boundaries in eit—state estimation approach," *Inverse Problems*, vol. 17, no. 6, p. 1937, 2001.

[16] S. Kim and A. K. Khambampati, *Mathematical concepts for image reconstruction in tomography*. Elsevier Ltd, 2015.

[17] A. K. Khambampati, K. Y. Kim, Y.-G. Lee, and S. Kim, "Boundary element method to estimate the time-varying interfacial boundary in horizontal immiscible liquids flow using electrical resistance tomography," *Applied Mathematical Modelling*, vol. 40, no. 2, pp. 1052–1068, 2016.

[18] A. Rashid, S. Kim, D. Liu, and K. Kim, "A dynamic oppositional biogeography-based optimization approach for time-varying electrical impedance tomography," *Physiological measurement*, vol. 37, no. 6, p. 820, 2016.

[19] S. Ren, M. Soleimani, Y. Xu, and F. Dong, "Inclusion boundary reconstruction and sensitivity analysis in electrical impedance tomography," *Inverse Problems in Science and Engineering*, vol. 26, no. 7, pp. 1037–1061, 2018.

[20] S. Ren, Y. Wang, G. Liang, and F. Dong, "A robust inclusion boundary reconstructor for electrical impedance tomography with geometric constraints," *IEEE Transactions on Instrumentation and Measurement*, no. 99, pp. 1–12, 2018. [Online]. Available: DOI: 10.1109/TIM.2018.2853358

[21] O.-P. Tossavainen, M. Vauhkonen, L. Heikkinen, and T. Savolainen, "Estimating shapes and free surfaces with electrical impedance tomography," *Measurement Science and Technology*, vol. 15, no. 7, p. 1402, 2004.

[22] S. Ren, Y. Xu, C. Tan, and F. Dong, "Reconstructing the geometric configuration of three dimensional interface using electrical capacitance tomography," *International Journal for Numerical Methods in Engineering*, vol. 96, no. 10, pp. 628–644, 2013.

[23] S. Babaeizadeh and D. H. Brooks, "Electrical impedance tomography for piecewise constant domains using boundary element shape-based inverse solutions," *IEEE transactions on medical imaging*, vol. 26, no. 5, pp. 637–647, 2007.

[24] D. Watzenig, M. Brandner, and G. Steiner, "A particle filter approach for tomographic imaging based on different state-space representations," *Measurement Science and Technology*, vol. 18, no. 1, p. 30, 2006.

[25] E. Somersalo, M. Cheney, and D. Isaacson, "Existence and uniqueness for electrode models for electric current computed tomography," *SIAM Journal on Applied Mathematics*, vol. 52, no. 4, pp. 1023–1040, 1992.

[26] P. Vauhkonen, M. Vauhkonen, T. Savolainen, and J. Kaipio, "Three-dimensional electrical impedance tomography based on the complete electrode model," *IEEE Trans. Biomed. Eng*, vol. 46, pp. 1150–1160, 1999.

[27] V. Kolehmainen, S. Arridge, W. Lionheart, M. Vauhkonen, and J. Kaipio, "Recovery of region boundaries of piecewise constant coefficients of an elliptic pde from boundary data," *Inverse Problems*, vol. 15, no. 5, p. 1375, 1999.

[28] J. Avery, T. Dowrick, M. Faulkner, N. Goren, and D. Holder, "A versatile and reproducible multi-frequency electrical impedance tomography system," *Sensors*, vol. 17, no. 2, p. 280, 2017.

[29] J. Kourunen, T. Savolainen, A. Lehikoinen, M. Vauhkonen, and L. Heikkinen, "Suitability of a pxi platform for an electrical impedance tomography system," *Measurement Science and Technology*, vol. 20, no. 1, p. 015503, 2009.

[30] T. J. Yorkey, J. G. Webster, and W. J. Tompkins, "Comparing reconstruction algorithms for electrical impedance tomography," *IEEE Transactions on Biomedical Engineering*, no. 11, pp. 843–852, 1987.

[31] K. Karhunen, A. Seppänen, A. Lehikoinen, P. J. Monteiro, and J. P. Kaipio, "Electrical resistance tomography imaging of concrete," *Cement and Concrete Research*, vol. 40, no. 1, pp. 137–145, 2010.

[32] C. Harmening and H. Neuner, "Choosing the optimal number of b-spline control points (part 1: Methodology and approximation of curves)," *Journal of Applied Geodesy*, vol. 10, no. 3, pp. 139–157, 2016.

[33] M. Wen, S. Whalen, R. Elliott, and E. Tadmor, "Interpolation effects in tabulated interatomic potentials," *Modelling and Simulation in Materials Science and Engineering*, vol. 23, no. 7, p. 074008, 2015.

[34] D. Salomon, *Curves and surfaces for computer graphics*. Springer Science & Business Media, 2007.

[35] S. J. Hamilton and A. Hauptmann, "Deep d-bar: Real time electrical impedance tomography imaging with deep neural networks," *IEEE Transactions on Medical Imaging*, vol. 37, no. 10, pp. 2367–2377, 2018.

[36] Z. Yan, S. Schiller, G. Wilensky, N. Carr, and S. Schaefer, "k-curves: interpolation at local maximum curvature," *ACM Transactions on Graphics (TOG)*, vol. 36, no. 4, p. 129, 2017.

[37] L. M. Heikkinen, T. Vilhunen, R. M. West, and M. Vauhkonen, "Simultaneous reconstruction of electrode contact impedances and internal electrical properties: Ii. laboratory experiments," *Measurement Science and Technology*, vol. 13, no. 12, p. 1855, 2002.

[38] A. Nissinen, L. Heikkinen, V. Kolehmainen, and J. Kaipio, "Compensation of errors due to discretization, domain truncation and unknown contact impedances in electrical impedance tomography," *Measurement Science and Technology*, vol. 20, no. 10, p. 105504, 2009.

[39] G. Boverman, D. Isaacson, J. C. Newell, G. J. Saulnier, T.-J. Kao, B. C. Amm, X. Wang, D. M. Davenport, D. H. Chong, R. Sahni *et al.*, "Efficient simultaneous reconstruction of time-varying images and electrode contact impedances in electrical impedance tomography," *IEEE Transactions on Biomedical Engineering*, vol. 64, no. 4, pp. 795–806, 2017.

[40] C. Gómez-Laberge and A. Adler, "Direct eit jacobian calculations for conductivity change and electrode movement," *Physiological measurement*, vol. 29, no. 6, p. S89, 2008.

[41] X. Li and Y. Chang, "Non-uniform interpolatory subdivision surface," *Applied Mathematics and Computation*, vol. 324, pp. 239–253, 2018.

[42] N. Vu-Bac, T. Duong, T. Lahmer, X. Zhuang, R. Sauer, H. Park, and T. Rabczuk, "A nurbs-based inverse analysis for reconstruction of nonlinear deformations of thin shell structures," *Computer Methods in Applied Mechanics and Engineering*, vol. 331, pp. 427–455, 2018.

[43] A. Nissinen, V. P. Kolehmainen, and J. P. Kaipio, "Compensation of modelling errors due to unknown domain boundary in electrical impedance tomography," *IEEE Transactions on Medical Imaging*, vol. 30, no. 2, pp. 231–242, 2011.

[44] D. Liu, V. Kolehmainen, S. Siltanen, and A. Seppänen, "A nonlinear approach to difference imaging in eit; assessment of the robustness in the presence of modelling errors," *Inverse Problems*, vol. 31, no. 3, p. 035012, 2015.

[45] D. Liu, V. Kolehmainen, S. Siltanen, A.-M. Laukkanen, and A. Seppänen, "Nonlinear difference imaging approach to three-dimensional electrical impedance tomography in the presence of geometric modeling errors," *IEEE Transactions on Biomedical Engineering*, vol. 63, no. 9, pp. 1956–1965, 2016.